Available online at www.sciencedirect.com
ScienceDirect
Journal of the European Ceramic Society 28 (2008) 1451–1466
www.elsevier.com/locate/jeurceramsoc

Constrained sintering: A delicate balance of scales

David J. Green [a,*], Olivier Guillon [b], Jürgen Rödel [b]

[a] *Department of Materials Science and Engineering, The Pennsylvania State University, PA 16802, USA*
[b] *Materials Science, Technische Universität Darmstadt, Darmstadt D-64287, Germany*

Available online 22 January 2008

Abstract

Sintering is a common technique for the production of ceramic, metallic and composite bodies and components. During this process it is known that internal stresses can arise from external constraint or from differential densification. These stresses can give rise to significant strain rate changes, distortions and damage in the fired parts. For quality control of sintered bodies, it is necessary to measure or predict the changes in deformation behaviour that occurs as the porous starting bodies undergo densification. Contributions of the continuum mechanical approach to this problem of constrained sintering are reviewed. Theoretical predictions as well as experimental techniques and results are detailed. Special emphasis is given to the development of anisotropy that can develop in the microstructure of a sintering body in response to the internal stresses.

Keywords: Films; Sintering; Microstructure; Porosity; Mechanical modelling

1. Introduction

Sintering is a common means for producing materials in a useful and robust form, especially ceramics, and involves heating a powder assemblage or other porous structures. The porous structure usually undergoes densification and strengthening, as well as developing other required functions. Sintering is also a technology and science with ancient roots that has increased in complexity in both structure and function. For example, compare the clay pottery produced in the early Chinese dynasties to the integrated co-fired electronic packages being produced today. In early societies, 'fired' ceramics were not only important for their function but also as a means of expression and status. Today the emphasis is often more on the commercial use of sintered materials as components in complex engineering structures.

From a technological point of view, it is critical to understand how to control the sintering process and to ensure that reproducible materials of high quality are obtained. Understanding the mechanisms involved in the sintering process is clearly an important strategy for obtaining this control. In the last 50 years, there have been significant developments in understanding sintering mechanisms and there has been great success in integrating this theory for all scale levels, from the atomistic to the macroscopic. In the last 25 years, attention turned to situations in which internal stresses develop during the densification process as a result of mismatch in the sintering rates within the sintering body or component. An important development was the use of continuum mechanics to describe the deformation behaviour of porous bodies and to predict the stresses and strains that can develop from strain incompatibilities. Clearly, this is an important approach if these stresses and strains can be linked to damage or distortion that can occur during the sintering process and, hence to the quality and yield of the final product. Although continuum mechanics would seem to ignore structure, it has been shown that the scale levels can be linked. For example, it is possible to link the mechanisms of atomic motion with the basic thermodynamic driving forces, extrinsic factors, such as temperature and the changing thermo-mechanical properties of the porous material as the porous structure changes. Moreover, for accurate modelling and simulations, the structure must be described at multiple scale lengths. For example, in crystalline materials, the atomistic, crystalline, pore structure, phase geometries and component shape would all be linked.

One of the difficulties with the above approach is that the internal stresses that develop within a sintering body will change the structure and hence the densification rate. This perturbation leads to a 'stress memory' effect that will lead to anisotropy of the sintering behaviour, producing new challenges for both the theorist and experimentalist. The aim of this review is to describe developments in sintering theory, especially those using

* Corresponding author. Tel.: +1 814 863 2011; fax: +1 814 865 2917.
E-mail address: green@ems.psu.edu (D.J. Green).

0955-2219/$ – see front matter © 2007 Elsevier Ltd. All rights reserved.
doi:10.1016/j.jeurceramsoc.2007.12.012

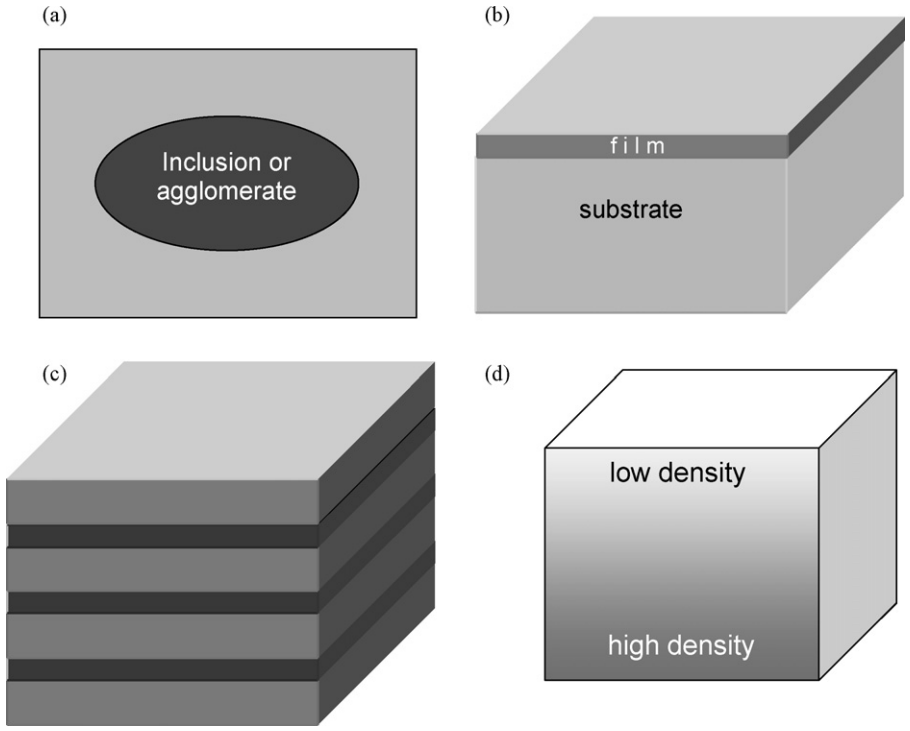

Fig. 1. Schematic illustrations of structures that will undergo differential densification: (a) Composite materials in which a porous matrix densifies around rigid inclusions, (b) a thin film densifying on a non-densifying substrate, (c) Layered structures of two or more types of materials that densify at different rates, (d) a porous material that has density variations. For powders containing agglomerates the inclusion in (a) can replaced by an agglomerate that densifies at a different rate than the surrounding material.

continuum mechanics to describe constrained sintering. The recent developments in the experimental methodology used to characterize the deformation behaviour and, the influence of the anisotropy in the sintering process will also be described. Finally, the new challenges to the theory and practice of constrained sintering will be outlined.

2. Sintering theory and constrained densification

The main foundations of sintering theory were laid from the late 1940s to the 1960s. These developments are now described in several textbooks and reviews.[1–7] In these advancements, particle models were devised based on identified mechanisms of atomic motion. These theories linked atomic fluxes associated with the sintering process to the thermodynamic parameters, the consolidation behaviour and grain growth, thus integrating the understanding at different scale levels. In addition, it was important to incorporate the structural transition from open to closed porosity as the pore structure is changed and removed.

An important concept during these developments was that of sintering potential. The sintering potential in isotropic densification is equivalent to the hydrostatic stress that is sufficient to halt the densification process and hence reflects the driving force for sintering, i.e., the reduction of interfacial energy. For the sintering of ceramics, sintering can occur in the solid state or can be aided by the presence of a liquid. In both cases, the atom transport is often associated with diffusion processes. An important development was that diffusional sintering mechanisms could be viewed as a creep process, which allows for the incorporation of continuum mechanics into the methodology (see Olevsky[8]).

The trouble with early sintering theory was that it was usually limited to two particle models. In the early 1980s, this lack of complexity compared to real particle packing was seen as a major obstacle to further theoretical developments. There has, however, been significant progress in numerical simulation of the sintering process, as pioneered by Riedel and co-workers and applied recently by Kraft and Riedel[9] to real sintering bodies. These types of simulations can also incorporate simultaneous sintering mechanisms and external factors, such as gravity, temperature gradients and friction. Numerical simulations have the potential to deal with more complex particle packing geometries and the sintering structure can be described at multiple and integrated scale levels. The simulations can also be coupled to models or experimental data for green body structure. In recent times, improved tools are also being developed for *in situ* observation of the sintering process, such as X-ray computed tomography.[10]

In the 1980s, new challenges for sintering science appeared with the interest in structural ceramics and the need to develop improved materials. The main paradigm was to develop composite materials with the addition of particles, whiskers or fibres to produce ceramic matrix composites with increased fracture toughness and strength.[11] Clearly, this meant there was a technological necessity to sinter composite materials. In the area of functional ceramics, there was an interest in using ceramics in the rapidly expanding microelectronic industry, in communication devices and as sensors and actuators. From this the

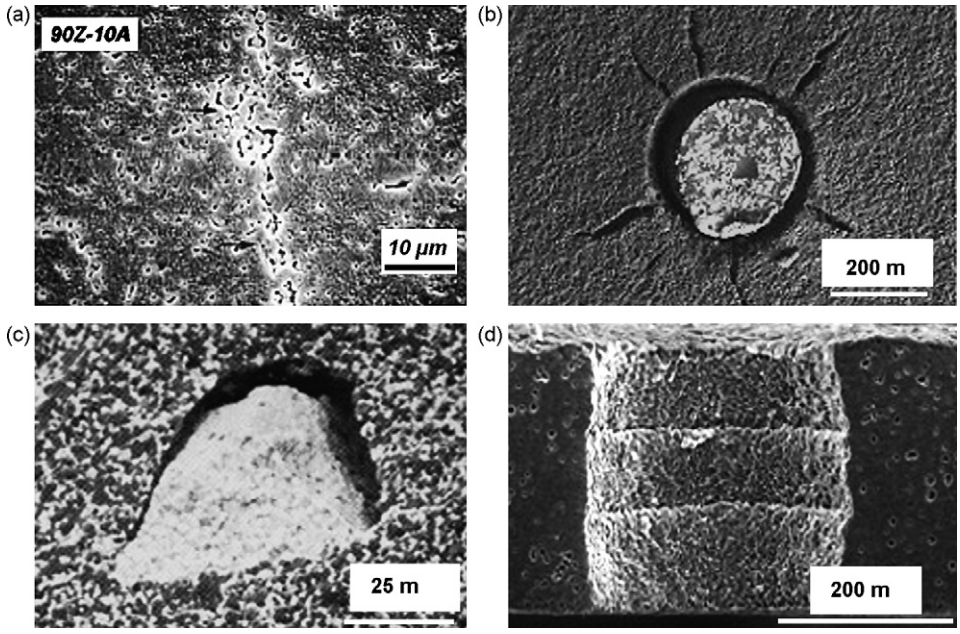

Fig. 2. Examples of damage and distortion in sintering structures: (a) cavity formation during the densification of an alumina-zirconia laminate, adapted from Cai et al.[13] (b) Sintering damage around a metal via after co-firing with a ceramic dielectric, micrograph courtesy of Aravind Mohanram. (c) Failure origin in an alumina-zirconia composite caused by an agglomerate that densified more rapidly than the surrounding material. (d) Hole distortion in low-temperature co-fired ceramic after being subjected to surface constraint, micrograph courtesy of Aravind Mohanram.

need to sinter ceramics in some complicated geometric patterns, such as thin films or layered structures arose, often in miniaturized form. The combinations of multiple materials into a single device meant, there was an economic incentive to simultaneously sinter (co-fire) the materials. The development of the sintering process for multilayer capacitors, in which ceramic dielectric and metal electrodes are co-fired, is a good example. In more recent times, microelectronic packages with complex 3D structures and ceramic micro-systems need to be co-fired.[12]

The above developments produced a new set of challenges for sintering theory, particularly when parts of a structure densify at different rates and temperatures than other parts (differential densification) or if the sintering is externally constrained (constrained densification). These problems are illustrated in Fig. 1. In the sintering of composites, a porous matrix is often required to densify around the second phase material that can be present in a variety of geometric forms, e.g., particles, whiskers, platelets or rods (Fig. 1(a)). Thus, the matrix is densifying onto rigid reinforcements. The reinforcement is placed under a compressive stress and the mean stress in the matrix is tensile. A similar situation arises when a ceramic film densifies by sintering on a rigid substrate (Fig. 1(b)). In this case, the sintering film will be placed in biaxial tension by the substrate and the densification can only occur in vertical direction. In layered structures that are co-fired, the layers will usually try to shrink at different rates and the layers will constrain each other, again leading to internal stresses (Fig. 1(c)). A more generic source of internal stress can occur even in a single-phase material system and is a result of inhomogeneous powder packing in the green bodies (Fig. 1(d)). The differential sintering associated with these density variations leads to differential densification and, hence internal stresses. A further complication arises due to the presence of agglomerates in these compacts, which induces locally differential densification. For example, an agglomerate that densifies faster or slower than the surrounding matrix could replace the inclusion depicted in Fig. 1(a).

For all the above self-stressed systems, there must be a force balance at all times. For example, in Fig. 1(b), the film is in tension and there is a compensating compression in the substrate. In all these examples, the internal stresses have the potential to hinder densification or lead to defects and/or distortions in the fired bodies. Some examples of damage and distortion that resulted from constrained sintering are shown in Fig. 2. It is also important to understand that self-stresses arise in multi-component bodies during the cooling stage of the sintering process, usually in the form of residual stresses. These stresses usually result from mismatches in the thermal expansion behaviour of the various components or from other types of strain mismatch and can be orders of magnitude greater than the stresses that occur during densification. Cooling stresses in ceramics are usually described using linear elasticity and can be high enough to initiate various modes of fracture or permanent deformation. For the success of the sintering process, the cooling stresses must be controlled but their discussion is beyond the scope of the present review.

3. Continuum mechanical description of sintering

There has been substantial effort to develop constitutive models to understand differential sintering. Many early approaches assumed the sintering material to be viscoelastic. As with sintering theory, the similarity of constrained sintering to the creep process allowed continuum mechanics to be used with the need to incorporate the changing microstructure. Bordia and Scherer[14–16] critically examined these viscoelastic models and

suggested that it would be more appropriate to use a constitutive equation based on linear viscous deformation. They argued that the viscoelastic treatment is not only inapplicable but also even unnecessary. While it is reasonable to assume that the sintering compact is viscoelastic, the elastic component is rather small during densification given the densification strains are enormous compared with the elastic strains. Moreover, the observed deformation results entirely from flow or creep. In fact, studies showed that the elastic response showed only a transient rise in stress and the stress at the end of the transient would be the same as that calculated from a purely viscous analysis. Bordia and Scherer concluded that a viscoelastic analysis is unnecessary.[14] This conclusion significantly simplifies the theoretical underpinning for modelling and for performing experimental measurements. As shown by Cai et al.,[17] the experimental measurements support this concept.

3.1. Isotropic formulation

For a linear viscous material, the strain rate components are linearly proportional to the stress components and traditionally four viscosity constants are defined, the shear (G_p) and bulk viscosities (K_p) or the uniaxial viscosity (E_p) and viscous Poisson's ratio (ν_p). These parameters will be termed viscous constants but they are only constant for a defined temperature and a specific microstructure with the microstructure continuously changing during the sintering process. The deformation behaviour can then be defined in terms of any two of these constants. For an isotropic, linear viscous material, Newton's Law for the principal stresses ($\sigma_1, \sigma_2, \sigma_3$) and principal strain rates ($\dot{\varepsilon}_1, \dot{\varepsilon}_2, \dot{\varepsilon}_3$) can be written as

$$\begin{aligned}\dot{\varepsilon}_1 &= \dot{\varepsilon}_f + \frac{1}{E_p}(\sigma_1 - \upsilon_p[\sigma_2 + \sigma_3])\\ \dot{\varepsilon}_2 &= \dot{\varepsilon}_f + \frac{1}{E_p}(\sigma_2 - \upsilon_p[\sigma_1 + \sigma_3])\\ \dot{\varepsilon}_3 &= \dot{\varepsilon}_f + \frac{1}{E_p}(\sigma_3 - \upsilon_p[\sigma_1 + \sigma_2])\end{aligned} \quad (1)$$

These equations are analogous to Hooke's law for linear elastic, isotropic continua, with strain rate replacing strain and the addition of the intrinsic free sintering strain rate, $\dot{\varepsilon}_f$.

Based on the linear viscous assertion, one needs to measure or calculate these viscosity quantities for any point in an arbitrary sintering cycle. The above equations can also be used to determine the relationship between the viscosity constants and the sintering potential, Σ. By setting the principal strain rates to zero and using $\sigma_1 = \sigma_2 = \sigma_3 = \Sigma$ in Eq. (1), one obtains

$$\Sigma = -\frac{E_p \dot{\varepsilon}_f}{1 - 2\upsilon_p} \quad (2)$$

Eq. (2) is a critical equation as it allows the viscosity parameters to be related to the thermodynamic driving forces, notably the surface energy and pore curvature. In addition, Eq. (2) can be used to measure the sintering potential from experimental measurements of the viscosity constants.

There are numerous theoretical expressions for the viscosity constants in Eq. (1). These models usually relate the viscosity constants to temperature, relative density and (if polycrystalline) grain size. It is not, however, appreciated that the green density will also influence these constants since the densification of the porous structure can proceed in a variety of ways from differing starting pore structures. In addition, other processes, such as crystallization[18] or chemical reactions may occur simultaneously with densification. The theoretical approaches can be broadly classified into phenomenological and micromechanical models.

The micromechanical models are usually based on an elementary cell, composed generally of a contact between two particles or an isolated pore in a matrix. The sintering mechanisms are then introduced, e.g., grain boundary diffusion, surface diffusion and volume diffusion for crystalline solids, viscous flow for amorphous solids, contact flattening for liquid phase sintering, etc. The authors then predict the cell behaviour during free sintering or under an external stress. For instance, Scherer[19,20] proposed expressions for E_p and ν_p as functions of relative density for low-density glasses based on a microstructural model consisting of cubic unit cells of cylindrical particles. The model did not take into account grain growth and assumed a specific geometric arrangement of the pores. Similarly, Mackenzie and Shuttleworth[21] derived expressions for shear (G_p) and bulk viscosities (K_p), based on a spherical shell model. Skorokhod,[22] Bassani[23] Qian et al.[24] suggested expressions for effective shear and bulk viscosities using self-consistent methods. Other micromechanical models, such as those of McMeeking and Kuhn,[25] Cocks,[26] Swinkells and Ashby,[27] Helle et al.,[28] Riedel et al.,[29,30] and Jagota et al.[31] consider the different stages of sintering, such as the initial, intermediate and final stages, and take into account the interaction between grain growth and densification. For example, Riedel et al.[29,30] derived expressions for the intermediate and final stages of sintering based on an analysis for three different grain arrangements assuming grain-boundary diffusion as the predominant creep mechanism. Kraft and Riedel[9] have recently reviewed the various refinements to this approach. Du and Cocks[32] developed a general constitutive model for different stages of sintering incorporating grain growth with creep and the densification model of Hsueh et al.[33] Bordia and Scherer[14] indicated several problems with the Hsueh et al. analysis,[33] primarily that the underlying experimental data was not equivalent to a realistic sintering structure as the pores were artificially introduced. Finally, some micromechanical models have considered the statistics of particle contacts.[28,34] In summary, the correlation between viscosity parameters and atomic transport mechanism has been provided for intermediate and final stage sintering for the case of simple, well described, isotropic powder packing structures. Initial stage sintering, including rearrangement, has not yet been covered as successfully.

In addition to these analytical models, sinter-forging techniques were used to determine how viscosity varies as a function of relative density for glasses, ceramic-filled glasses and polycrystalline ceramics. Models derived from these data constitute the empirical approach for developing constitutive equations for

sintering. In these studies, a loading dilatometer under constant load was used to study simultaneously the creep and densification of a porous sample and thus, calculate the shear and bulk viscosities. De Jonghe, Rahaman et al.[35–40] and Raj et al.[41–44] performed most of these studies in the late 1980's. Raj and Bordia[41] assumed explicit spring-dashpot elements to represent the constitutive properties of a porous material. As pointed out later by Bordia and Scherer,[15] this analysis[41] has several limitations, most importantly that the shear viscosity is assumed to be constant. Generally, De Jonghe, Rahaman et al.[35–40] and Raj et al.[41–44] concluded that the strain rate varies linearly with the stress.

Bordia and Scherer[15] have compared several of the above models and noted they all predict differing dependencies of the viscosities on the relative density, especially the shear viscosity. Gillia[45] recently performed a similar comparison. Bordia and Scherer[15] also pointed out that several of the theoretical expressions for the viscosity constants (i.e., Refs. 22, 33 and 43) predict a negative viscous Poisson's ratio in contradiction to the experimental data and this leads to the prediction of high stresses during sintering. The problems with the theoretical expressions for the viscosity constants have made them very difficult to apply. Gillia et al.[46] have echoed the same sentiment more recently. Chang et al.[47] recently measured the uniaxial viscosity of Gd-doped ceria. The experimental data were best predicted by the expression of Rahaman et al.[37] Good agreement was also found with the models of Riedel et al.[29,30] and Hsueh et al.[33] Bordia and Scherer[14] also questioned the use of sinter forging to obtain the viscosity constants, as the application of a continuous uniaxial load could lead to anisotropy in the microstructure. In later sections, we will show that microstructural anisotropy does occur when stresses are applied to a sintering material. In addition, the development of new experimental tools for measuring the viscosity constants will also be described.

3.2. Modes of constraint

Once the viscosity constants are known for component materials in a sintering structure there is still the need to couple this information with the linear viscous solution for the geometry of sintering structure. Solutions for the four constraint geometries shown in Fig. 1 will be discussed in the following.

3.2.1. Sintering around inclusions

As mentioned earlier, constrained sintering arises locally in the sintering of composites since one is usually adding 'non-densifying' inclusions to a matrix that densifies. In this situation, the mean stress will be compressive on the inclusion and tensile on the matrix, thereby opposing densification. The internal stress field will also depend on the shape of the second phase and its volume fraction. In agreement with this simple description, studies[48–51] confirmed the densification rate decreases with increasing volume fraction of inclusions and that densification apparently ceases before the theoretical density is reached. Percolation theory[52,53] was found to be relevant to the constrained sintering of composites. Above the percolation threshold, the second phase forms a continuous network that will act like a skeleton and will severely inhibit densification. For example, in the sintering of composites, such as depicted in Fig. 1(a), the problem is often modelled as a linear viscous matrix being sintered around the inclusion. Bordia and Scherer discussed this analysis in depth[16] so there is no need to duplicate this debate here.

3.2.2. Co-firing of laminates

Other important stress solutions are those associated with layered structures. They all derive from the fact that the integrals of stresses and bending moments along the thickness direction z should be equal to zero for a multilayer in mechanical equilibrium without the application of external forces. For example, Cai et al.[13,54] considered a symmetric laminate consisting of alternating layers of two sintering materials. Using the infinite plate solution for linear viscous, densifying materials, it was shown[54] that the equi-biaxial stresses that arise in the layers are given by

$$\sigma_1 = \frac{1}{1+mn} E'_{\mathrm{p1}} \Delta\dot{\varepsilon} \tag{3}$$

where

$$m = \frac{t_1}{t_2}, \quad n = \frac{E'_{\mathrm{p1}}}{E'_{\mathrm{p2}}} \tag{4}$$

where t is the layer thickness, $\Delta\dot{\varepsilon} = \dot{\varepsilon}_2 - \dot{\varepsilon}_1$ the mismatch of strain rates between the layers, $E'_{\mathrm{p}} = E_{\mathrm{p}}/(1-\nu_{\mathrm{p}})$ for plates and $E'_{\mathrm{p}} = E_{\mathrm{p}}$, for beams and the subscripts refer to layer 1 or 2. The above solution is obtained by setting the strain rates in the two layers equal to each other and maintaining a force balance for the compensating tensile and compressive stresses in the two layers. For example, if layer 1 is shrinking faster than layer 2, then layer 1 will be in equi-biaxial tension and layer 2 in equi-biaxial compression.

Cai et al.[54] used the above analysis to calculate the stresses that arise in the densification of alumina/zirconia laminates and how the densification stresses could be reduced by changing the composition of the layers. It was also shown[30] that the stresses during densification would be the same even if the layers were considered to be viscoelastic. In order to confirm the stress calculations, Cai et al.[13,54] performed experiments on alumina/zirconia bi-layers. The asymmetry in these laminates allows the structure to bend in response to the stresses that arise. For example, the layer that shrinks faster will be in tension but this stress can be relaxed by bending of the bi-layer. The normalized degree of curvature, k, of the bi-layer was predicted using Ref. 54:

$$k = \frac{t_1 + t_2}{r} = \frac{6(m+1)^2 mn}{m^4 n^2 + 2mn(2m^2 + 3m + 2) + 1} \cdot \Delta\dot{\varepsilon} \tag{5}$$

where r is the radius of curvature. Eqs. (4) and (5) are very useful as they show which factors control stress evolution and distortion in layered structures and, thereby indicate routes for their mitigation by microstructural design changes.

Using a different approach, Kanters et al.[55] argued that a bi-layer geometry can be described using Kirchhoff thin plate theory description under the assumption that the global thickness

remains small compared to the radius of curvature and that edge effects can be neglected. No stress develops in the thickness direction, z, and the bi-layer is under a biaxial stress state. Radial strain rate as a function of position along z is given by

$$\dot{\varepsilon}_r(z) = \dot{\varepsilon}_0 - z\dot{\kappa} - \dot{z}\kappa \tag{6}$$

where $\dot{\varepsilon}_0$ is the strain rate for $z=0$ and κ the inverse of curvature radius. Then the radial stress can be computed through the thickness:

$$\sigma_r(z) = \frac{E_p(z)}{1-\nu_p(z)}(\dot{\varepsilon}_0 - z\dot{\kappa} - \dot{z}\kappa - \dot{\varepsilon}_f(z)) \tag{7}$$

Curvature rate and in-plane strain rate are then obtained by solving the force and moment equilibriums. These approaches to predicting stress in bi-layers explicitly include the evolution of sintering viscosity during densification and grain growth as well as the evolution of sintering stress and its interaction with compatibility stresses for the different layers.

3.2.3. Sintering of thin films

Bordia and Raj[56] studied the sintering of thin ceramic films on rigid substrates and presented a model using phenomenological descriptions of the densification and shear properties. Scherer and Garino[57] and Hsueh[58] performed similar contemporary analyses. Assuming the densifying film is linear viscous, Eq. (1) can be used to calculate the stresses that arise from sintering on a rigid substrate. If the film is totally constrained in the x_1–x_2 plane, then $\dot{\varepsilon}_1 = \dot{\varepsilon}_2 = 0$ and the film stress, σ_f, is easily derived from Eq. (1) as

$$\sigma_f = -\frac{E_p\dot{\varepsilon}_f}{1-\nu_p} \tag{8}$$

The strain rate in the non-constrained direction, $\dot{\varepsilon}_3$, also follows and it depends only on υ_p and the unconstrained strain rate, i.e.

$$\dot{\varepsilon}_3 = \dot{\varepsilon}_f\left(\frac{1+\nu_p}{1-\nu_p}\right) \tag{9}$$

Jagota and Hui[59,60] have taken into account the sliding of a film on a substrate, introducing an equivalent friction coefficient for the interface. This coefficient depends on film thickness and nature of substrate. Under certain assumptions constrained sintering may also be used to determine viscous Poisson's ratio as shown by Mohanram et al.[61] on LTCC tapes.

At the microscopic scale, a few attempts have been made to simulate the evolution of particle geometry under constraining conditions. A geometrical model describing two constrained particles in contact volume conservation[62] highlighted the effect of dihedral angle and limited grain size on film densification. Wakai and Aldinger[63] used a surface evolver program to minimize surface and grain boundary energies to model the equilibrium shape of initially spherical identical particles for which the distance between mass centres is fixed. Similarly, Bordère et al.[64] developed a Monte Carlo approach to solve this problem for a viscous material.

Zhao and Dharani[65] and Olevsky et al.[66] have performed numerical simulations. Near the free edge, density is not uniform after sintering and a shape distortion is observed, the free upper corner having a higher density than the lower constrained corner. However, apart from the edge, the relative density is almost uniform. Nevertheless, this free edge effect could be more critical when sintering small features for which thickness is not negligible compared to their lateral dimensions. However, accuracy of the simulated behaviour of the constrained film compared with experimental values still needs to be addressed. Initial results obtained from thick ZnO bi-layers are encouraging.[66]

In layered structures, advantage has been taken of constrained sintering by attaching non-densifying layers to sintering films. These are termed 'zero-shrinkage structures,'[67,68] as no shrinkage occurs in the layer plane. This is a useful effect as it means tolerances are more easily kept within the plane when multiple layers are sintered. As with thin films, significant stresses will arise from the rigid constraint, the same as Eq. (9), making the layer more difficult to densify.[69,70] In addition and especially for rather thick structures, as the constraint is only applied along the surface of the sintering body, free surfaces, such as holes in the layers, will not be perfectly constrained, giving rise to curvature of free surfaces as shown earlier in Fig. 2(d). As shown by Tzeng and Jean[69] using finite element analysis (FEA), the tensile stresses that reduces the driving force for sintering decrease from the alumina/glass interface to the middle of the glass layer in the thickness direction and they also decrease near the free edges. These simulations were compared with experimental data (dimensions and local pore density) and showed a reasonable agreement.[69]

3.2.4. Green-density gradients

It is accepted that particles are inhomogeneously packed in green bodies and that differential sintering associated with these density variations leads to differential densification and possibly to the presence of defects or failure origins in the sintered material.[71–76] Fractography has shown that crack-like internal surfaces were the origin of failure,[74–76] as shown in Fig. 2(c). These internal surfaces developed as a result of differential sintering of agglomerates relative to their surrounding powder 'matrix'. Low-green-density regions are often found to sinter faster than high-density regions, which lead to internal stresses and damage. Thus, specimens containing low-green-density agglomerates could produce circumferential crack-like voids at the agglomerate/matrix interface. In contrast, agglomerates with a higher green density than the matrix will be subjected to compressive strains by the matrix and produced radial cracking around the agglomerate. Fig. 2(b) shows an example of a metal via co-sintered with a ceramic dielectric that shows both types of damage.

As co-sintered structures become more geometrically complex, it is clear that analytical stress solutions will not be available. The stress analysis then requires the use of finite element analysis (FEA), which has been pioneered by Riedel and co-workers, see recent review.[9] Olevsky et al.[66] has also used FEA extensively for sintering problems and recently combined

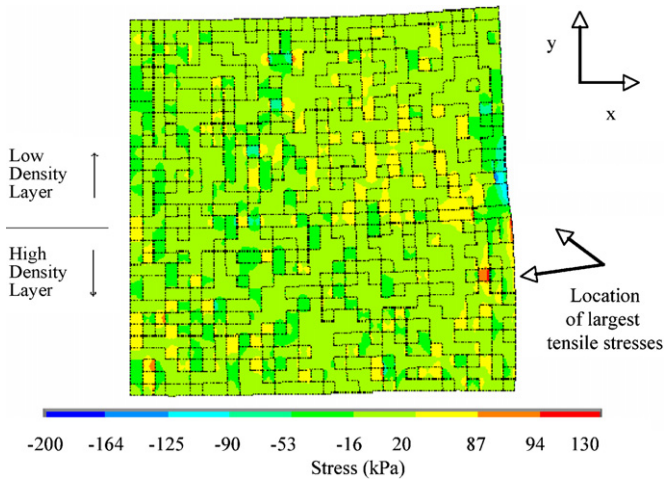

Fig. 3. Finite element analysis stresses of the by-layer sample for $BaTiO_3$ at 1300 °C: normal stress (x-direction) (adapted from Ref. 80).

this approach with mesoscale simulations of the sintering structure being developed by Tikare and co-workers.[77,78] Schoenberg et al.[79,80] recently used finite element analysis to calculate the stresses that occur as a result of variations in green density. The approach involved measurement of the viscosity constants as a function of green density combined with X-ray computed tomography to describe the density variations prior to sintering. The finite element analysis then allowed a simulation of the stresses and strains that occur in the densification process of a specific sample. This allowed regions of high stress to be identified and this was correlated to the observed damage,[80] as shown in Fig. 3. Ravi and Green[81] have used the analysis described earlier for bi-layers with differing green densities.

The advantage of FEA is that other effects, such as gravity, friction, thermal gradients, residual stresses, different powder packing geometries, simultaneous sintering mechanisms can be incorporated into the analysis. The disadvantage is that it becomes more difficult to identify the fundamental parameters that control the stress and strain rate evolution. Another major disadvantage is that there is little known about the damage mechanisms and the strength changes that occur during the sintering process. It is generally supposed that stresses during sintering should not exceed the sintering potential as sintering will cease but these stresses have not been linked to particular damage mechanisms. Finally, the emphasis in this paper has been the stresses that occur during densification. There are, however, processes, such as binder burnout and chemical reactions that can also produce stress in a sintering structure. Although the isotropic formulation has proved to be very useful in studying constrained sintering, it really only allows stresses to be predicted for small perturbations. As will be shown below, if a stress is applied continuously to a sintering material, the microstructure will become anisotropic, reflecting the deviatoric nature of the stresses. For example, if equi-biaxial compressive stresses arise during sintering, the interparticle necks will grow faster in the stress plane than normal to this plane. This stress-induced anisotropy will also be expected to change the magnitude of the sintering potential and the uniaxial viscosity in the stress directions.

3.3. Anisotropic formulation

Although sintering behaviour is often considered as isotropic for the sake of simplicity, it appears that in reality many sintering bodies shrink in an anisotropic manner.[82–86] This anisotropy is easily characterized at a macroscopic level by measuring the ratio of axial to radial dimensions, strains or strain rates. However, it may be difficult to link this macroscopic anisotropy to anisotropy in the microstructure. Indeed many characteristics of particle packing may have an effect on sintering anisotropy: alignment of anisometric particles, anisotropy in particle contact/pore curvature (also observable for spherical particles), anisotropy in surface energy (if a crystallographic orientation is available), presence of anisometric oriented inclusions, etc. Such anisotropic features in green packing are induced by the processing technique (e.g., tape casting, dip coating, uniaxial pressing and compaction, etc.). On the other hand, applied load,[87] internal stresses due to differential densification and constraining conditions[88] can act as sources of anisotropy as highlighted in Fig. 4, in which the radial and axial shrinkages are shown to differ after a sample has been subjected to an axial stress. In such cases, large deviations will be observed between isotropic predictions and real behaviour.

To take into account this anisotropic behaviour, the isotropic continuum mechanical framework presented in Part III can be generalized to the anisotropic case.[88] For an orthotropic material, principal strain rates $\dot{\varepsilon}_i$ are related to principal stresses σ_i according to

$$\dot{\varepsilon}_1 = \dot{\varepsilon}_1^{\mathrm{f}} + \frac{\sigma_1}{E_1^{\mathrm{p}}} - \frac{\nu_{21}^{\mathrm{p}}\sigma_2}{E_2^{\mathrm{p}}} - \frac{\nu_{31}^{\mathrm{p}}\sigma_3}{E_3^{\mathrm{p}}} \tag{10a}$$

$$\dot{\varepsilon}_2 = \dot{\varepsilon}_2^{\mathrm{f}} + \frac{\sigma_2}{E_2^{\mathrm{p}}} - \frac{\nu_{12}^{\mathrm{p}}\sigma_1}{E_1^{\mathrm{p}}} - \frac{\nu_{32}^{\mathrm{p}}\sigma_3}{E_3^{\mathrm{p}}} \tag{10b}$$

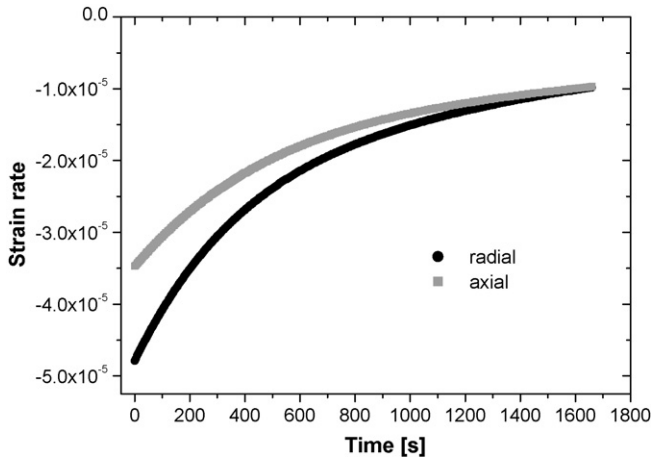

Fig. 4. Time dependence of axial and radial strain rates after load removal, for a pressure filtrated alumina compact sinter-forged up to ~75% density at 1150 °C. (load was constantly adjusted to prevent any radial shrinkage)[99].

$$\dot{\varepsilon}_3 = \dot{\varepsilon}_3^{\mathrm{f}} + \frac{\sigma_3}{E_3^{\mathrm{p}}} - \frac{\nu_{23}^{\mathrm{p}}\sigma_2}{E_2^{\mathrm{p}}} - \frac{\nu_{13}^{\mathrm{p}}\sigma_1}{E_1^{\mathrm{p}}} \tag{10c}$$

where E_i^{p} and ν_{ij}^{p} are the axial viscosities and viscous Poisson's ratios defined with respect to the principal directions. Some of the E_i^E and ν_{ij}^{p} values are related, i.e.

$$\frac{\nu_{12}^{\mathrm{p}}}{E_1^{\mathrm{p}}} = \frac{\nu_{21}^{\mathrm{p}}}{E_2^{\mathrm{p}}}; \quad \frac{\nu_{13}^{\mathrm{p}}}{E_1^{\mathrm{p}}} = \frac{\nu_{31}^{\mathrm{p}}}{E_3^{\mathrm{p}}}; \quad \frac{\nu_{23}^{\mathrm{p}}}{E_2^{\mathrm{p}}} = \frac{\nu_{32}^{\mathrm{p}}}{E_3^{\mathrm{p}}} \tag{11}$$

In the general anisotropic case, knowledge of three free strain rates ($\dot{\varepsilon}_i^{\mathrm{f}}$) and nine independent material parameters are required. In the specific case of transverse isotropy (as expected for sinter forged specimens and constrained films), only two free strain rates and five viscous constants are needed as discussed before in Ref. 88. Evolutions of anisotropic viscosities as well as viscous Poisson's ratio values have to be determined from models or experiments. The applicability range of these linear relationships has to be experimentally verified to assure that the anisotropic material behaves linearly for the whole range of stresses over to which the material is subjected.

Following expressions for the in-plane stress σ^{∞} and the constrained densification rate of the film $\dot{\varepsilon}_3^{\mathrm{constr.}}$ can be obtained from Eqs. (10a)–(10c) using $\dot{\varepsilon}_1 = \dot{\varepsilon}_2 = 0$, $\sigma_1 = \sigma_2$, $\sigma_3 = 0$, $E_1^{\mathrm{p}} = E_2^{\mathrm{p}}$, and $\nu_{13}^{\mathrm{p}} = \nu_{23}^{\mathrm{p}}$:

$$\sigma^{\infty} = -\frac{E_1^{\mathrm{p}}\dot{\varepsilon}_1^{\mathrm{f}}}{1-\nu_{12}^{\mathrm{p}}} \tag{12}$$

$$\dot{\varepsilon}_3^{\mathrm{constr.}} = \dot{\varepsilon}_3^{\mathrm{f}} + \frac{2\nu_{13}^{\mathrm{p}}}{1-\nu_{12}^{\mathrm{p}}}\dot{\varepsilon}_1^{\mathrm{f}} \tag{13}$$

where direction 3 is the film thickness direction.

Several micromechanical models have been developed to investigate the effect of an anisotropic microstructure on the macroscopic strain rate anisotropy. The general goal of these procedures is to predict the evolution of an initially anisotropic microstructure during free sintering. The first attempt was performed by Scherer and Garino[57] with a tube model for viscous sintering. Several configurations were considered by other researchers: anisotropy in coordination number of spherical particles by Jagota et al.,[89] elliptical oriented particles sintering by solid state diffusion or liquid phase sintering in 2D by Raj et al.[90] and asymmetric neck growth during the viscous sintering of a three-particle configuration, leading to particle rearrangement and anisotropic shrinkage by Zhou and Derby.[91] Olevsky[8] has reviewed the effect of pore size and morphology on anisotropic sintering. By considering ellipsoidal voids oriented in a continuous matrix,[93] shrinkage anisotropy results from the interplay between the tensoric nature of the Laplace pressure (a smaller radius of curvature leading to a larger sintering stress) and the introduction of anisotropic viscosities and Poisson's ratio. More recently, Olevsky and co-workers[93] modelled a 2D array of rectangular grains and elliptical pores placed at their corners. Aspect ratio of both features was considered to calculate explicitly anisotropic viscosities and sintering stresses. However these models are only valid for the last stage of sintering (i.e., densities above 92%). Similar problems can be treated in a more flexible way by means of 2D Monte Carlo methods.[94] Anisotropic sintering can then be studied starting from different and more realistic configurations. Ch'ng and Pan[95] focused on the evolution of an elongated pore in an isotropic polycrystalline dense matrix. As Olevsky and Skorohod predicted,[92] the representative volume shrinks more along the direction of the long pore axis. Other numerical simulation tools such as discretization of surface and grain boundary diffusion equations for particulate systems[84,96] or discrete element method[97,98] have been used to simulate anisotropic sintering after compaction under pressure as well as the effect of an applied stress during sintering,[99] enabling the determination of viscosities and Poisson's ratio of defined representative microstructures.

Even more pronounced than for isotropic sintering, difficulties are foreseen to link these different approaches to model the complete sintering of a powder compact to theoretical density. It is also expected that the 3D sintering behaviour of a real anisotropic material is different from that simplified in two dimensions. There are some reasons for that: it is particularly difficult to define 3D porosity anisotropy for example, because void spaces are linked together and still form a continuous network up to relatively high-density levels. Numerical models taking into account the arrangement of particles (like discrete element models) can to a certain extent give further insight in this topic. It may also be argued that the effect of external stress on shrinkage anisotropy is indirect: the mechanical stress induces anisotropy in the microstructure, which in turn affects densification rates in different directions after stress release. Therefore, 3D relationships describing the effect of stress on microstructure still need to be developed.

4. Measurement techniques

4.1. Sintering parameters

4.1.1. Measurement requirements

The continuum mechanical parameters for sintering are obtained by measuring strain rates at fixed applied stress for a specific material, density, grain size and temperature. Current equipment has a resolution of about 2 μm accuracy for determining dimensional changes, for a cylinder of 20 mm height and 12 mm diameter.[100] To reduce the effect of friction at the loaded ends and guarantee uniaxial stress state in the specimen, high-temperature lubricant such as boron nitride can be used and height/diameter ratio should be larger than 1.5. Recent experimental improvements addressed the problem of developing anisotropy[87] while a load during hot forging is applied. In order to obtain robust data points for an isotropic sintering material, with minimum effect on the microstructure, a compromise in hot forging has to be sought. A uniaxial load has to be applied long enough to get a strong signal above the background noise, but short enough that the microstructure remains essentially isotropic. Same consideration s can be applied to the stress amplitude (in the range of the sintering stress). Fortunately, the degree of anisotropic derailment can be quantified by assessing the axial and radial strain rates after the axial load has been

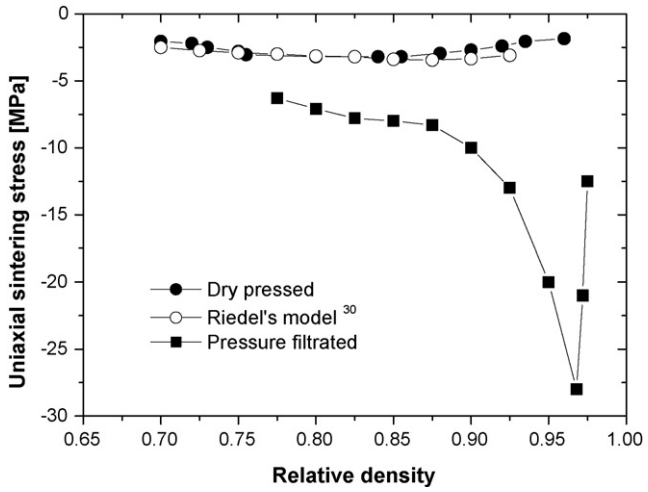

Fig. 5. Uniaxial sintering stress as a function of relative density for alumina compacts sintered at 1250 °C, produced by two different processing methods: dry pressing and pressure filtration.[108] Predictions given by Riedel et al.[30] are plotted for comparison.

removed.[87] Using this technique, the optimum duration for load application was found to depend on material, with alumina showing limited anisotropy after a load application over a 5% density increment,[101] but a LTCC material exhibiting large anisotropy after the same density increment under load.[102] This need for a compromise in the measurement technique has spawned two loading procedures, cycling loading dilatometry[17,46,103] and discontinuous hot forging.[47,102,104] Cycling loading dilatometry uses only short loading cycles to reduce anisotropy and to get many data points, while discontinuous hot forging applies a load only until unacceptable anisotropy has developed, thus obtaining only few, but robust values for a given specimen. Since the axial and radial strain rates are obtained in discontinuous hot forging, two or three load applications may be feasible during one sintering run, if the isotropic microstructure can be recovered to a sufficient degree.

4.1.2. Sintering potential

The sintering potential is related to grain size (or particle size in the case of amorphous materials), pore size, surface energy and grain boundary energy.[30,105] The experimental determination utilizes Eq. (2) and is based on an extrapolation of the linear relation between uniaxial stress vs. uniaxial strain rate towards a strain rate equal to zero. Submicron oxides like alumina exhibit sintering potentials of a few MPa, while nanocrystalline oxides like zirconia can exhibit sintering potentials of up to 100 MPa.[55,106] In contrast, LTCC materials render sintering potentials in the range of 0.1 MPa.[104] Temperature has no practical effect on the sintering potential through the minute changes in interfacial energies and small variations in the sintering trajectory as verified for the case of alumina.[107] The influence of density on sintering potential for the case of alumina is provided in Fig. 5, both for a uniaxially pressed alumina as well as for pressure-filtrated alumina.[108] During the intermediate stage sintering the sintering potential is found to increase. On transition from the intermediate stage of sintering to the final stage of sintering, the magnitude of the sintering potential decreases. This increase and decrease occurs at a later density and is much stronger for the case of pressure-filtrated specimens as compared to dry-pressed samples. The simulation in Fig. 5 is based on a combination of the intermediate and the final stage sintering models of Riedel and co-workers,[29,30] with the actual grain size used from the experiment. Theory therefore can only capture the transition from intermediate to final stage sintering in a rudimentary fashion. Further, since it relies on an initial assumption of powder packing, it cannot capture salient details in processing technology variations.

4.1.3. Sintering viscosities

The uniaxial viscosity conveniently is determined from Eq. (1) for the case where $\sigma_2 = \sigma_3 = 0$, where the slope of the linear relation between total active uniaxial sintering stress, σ_1, and uniaxial strain rate, $\dot{\varepsilon}_1$, is evaluated. Examples for measurements on gadolinium doped ceria[47] are provided in Fig. 6 and compared with data from an LTCC material.[102] For a polycrystalline material in general, the viscosity increases moderately until about 90% relative density[17,47,101,107] due to thickening of necks between grains and reduction of pore space and then increases strongly due to grain growth. In contrast, the increase in viscosity for the LTCC material appears less drastic as the grain growth contribution does not apply.[18,102] Note, that for the case of the LTCC material, crystallization changes the viscosity dramatically and is an important part in the design of LTCC materials.[18] For the case of crystalline materials, two models are also provided in Fig. 6 and demonstrate very good agreement. The correlation between macroscopic viscosity and atomic transport mechanism therefore is well treated in modelling. This fact can be further ascertained by comparing temperature dependent viscosity with temperature dependent diffusion data. The activation energies for the viscosity as measured using hot forging techniques and the activation energies for grain boundary diffusion were found to be in excellent agreement, as verified for alumina.[107] Problems with predictability for the uniaxial viscosity as a function of density may only arise for cases where

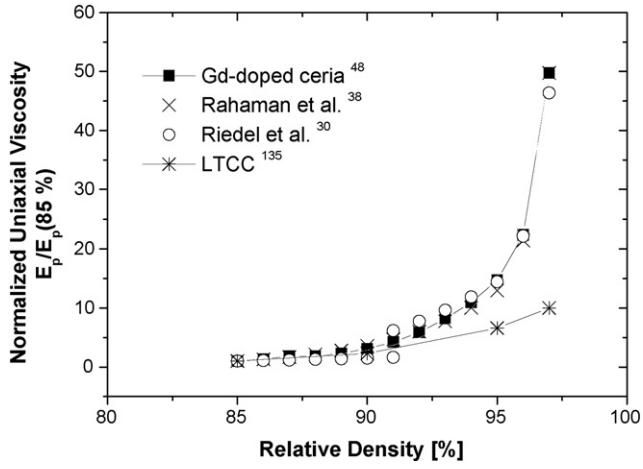

Fig. 6. Comparison between measured uniaxial viscosity normalized by density and theoretical predictions for a nanocrystalline Gd-doped ceria at 1100 °C and LTCC at 840 °C.

the grain size–density relationship, described as sintering trajectory, deviates from the common behaviour. Usually, grain growth is limited until about 90% of theoretical density, rather independent on sintering mechanism (liquid or solid state sintering) and applied pressure (free sintering or hot pressing).[110,111] Nanocrystalline powders, however, have a high-total surface energy, which can be reduced through elastic distortion of grains, and thus exhibit a higher tendency for agglomeration and differential sintering. Grain growth, therefore, ensues at lower densities than 90% TD in nanocrystalline materials,[112] thus impacting the viscosity–density relationship.[106]

4.1.4. Viscous Poisson coefficient

Determination of the viscous Poisson's coefficient has remained elusive for a long time and reliable data are still rare.[104,109] Application of a uniaxial load during hot forging can lead to anisotropy effects, thus thwarting good data for strain rates. This is particularly problematic for the determination of the viscous Poisson's coefficient, as its determination rests with the determination and then subtraction of small strain rates. From Eq. (1) for uniaxial tension, one finds

$$\nu_p = \frac{\dot{\varepsilon}_f - \dot{\varepsilon}_2}{\dot{\varepsilon}_1 - \dot{\varepsilon}_f} \tag{14}$$

where 2 and 1 refer to transverse and longitudinal axis, respectively. An alternative route of determining the viscous Poisson's coefficient has recently been applied for LTCC materials.[102] This method utilizes independent determination of the unaxial and the bulk viscosity and computes the viscous Poisson's coefficients by using the relationship between these two viscosities.

An example for three different sets of viscous Poisson's coefficients is provided in Fig. 7. For solid state sintering, it exhibits a close to linear dependence on density,[104,109,113] ranging from about 0.2 at green density to 0.5 at 100% TD. The case of the LTCC material, however, appears to be quite more complex (Fig. 7), with comparatively low values until 90% TD and then only a strong increase in viscous Poisson's coefficient. These

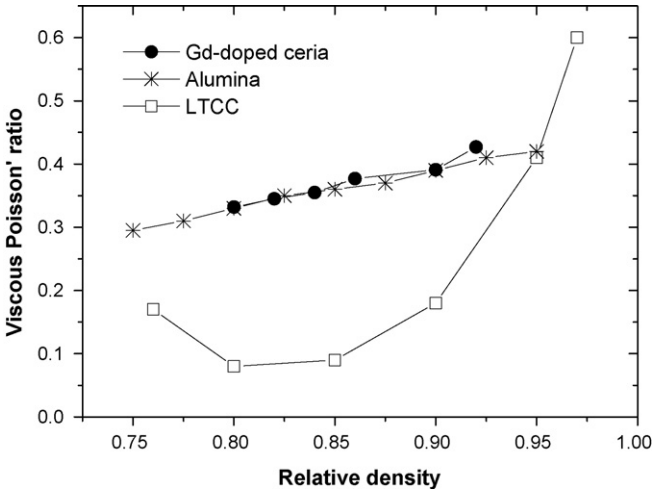

Fig. 7. Viscous Poisson's ratios as a function of relative density for three dry pressed materials: nanocrystalline Gd-doped ceria at 1050 °C,[113] alumina at 1250 °C[104] and LTCC glass ceramic composite at 840 °C.[102]

data have been rationalized with remnant effects of anisotropy, not only due to pore shape but also due to alignment of anisometric alumina particles.[104] An alternate route to determining the viscous Poisson's coefficient through hot forging relies on an evaluation of constrained sintering.[61] Eq. (9) provides a relation between the sintering rate under constraint as compared to free sintering through the viscous Poisson' coefficient. This method needs to determine the degree of anisotropy and makes the assumption that anisotropy does not change during constrained sintering.

4.2. Dimensional changes

4.2.1. Curvature measurements

For many applications control of lateral shrinkage and warpage is of highest importance. In microelectronics, final properties of the sintered components used in the radio frequency range are affected by geometric accuracy and flatness. Extensive experimental work has therefore been done in the field of low-temperature co-fired ceramics (LTCC) systems and solid oxide fuel cells (SOFC). LTCC components are composed of multilayered ceramics, composites and metals to build up 3D circuits,[114] whereas planar or tubular SOFC designs are made of anode and cathode separated by an electrolyte layer.[115] The technological goal is to minimize dimensional changes or at least to control them very precisely. Unfortunately, compatibility stresses arise from different densification rates (and at later stage different thermal expansion coefficients during cooling), which may induce delamination, cracking and also warping of the sintering part if the structure is asymmetric.

Typical experimental characterization tools are high-temperature optical dilatometers. They consist of a furnace equipped with transparent windows and a magnifying camera, which enables the direct observation of specimen shape and dimensional changes.[116] Additional filters and background lighting as well as image processing can be used to enhance image quality. It is then possible to measure curvature and distortion of multilayered ceramics during sintering.

Lu et al.[117,118] evaluated stresses for thin films sintering on a flexible non-sintering substrate. For example, a gold film or green LTCC tape deposited on silicon wafer was placed in a hot stage. A laser beam going through a quartz window was reflected by the curved surface and measured by an array detector. The in-plane stress was estimated from the curvature using a modified Stoney formula, to take into account the thickness changes of the film during densification:

$$\sigma = \frac{kE_s d_s^2}{6(1-\nu_s)d_0} \cdot \frac{\rho(t)^{1/3}}{\rho_0} \cdot \frac{d_s}{d_s + d_0(\rho_0/\rho(t))} \tag{13}$$

where E_s, ν_s, d_s are the Young's modulus, Poisson's ratio and thickness of substrate, $\rho(t)$ and ρ_0 are the instantaneous and initial film relative densities and d_0 the initial film thickness. Additional measurements of constrained film shrinkage are thus required. However, this equation only holds in case of thin coatings on a thick elastic substrate and the film properties are neglected. The use of a bending substrate to evaluate the stresses

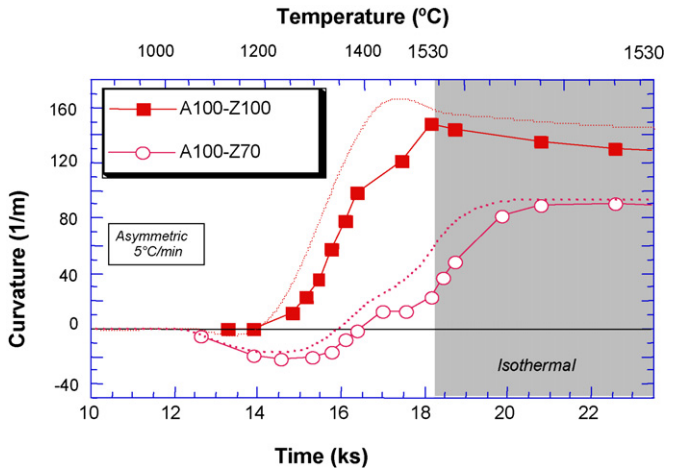

Fig. 8. Simulated (dashed line) and measured (solid line) curvature as a function of time for two different structures (A100 standing for pure alumina and Z100 for pure zirconia, whereas Z70 is a mixture of 70 wt.% ZrO_2 and 30 wt.% Al_2O_3) (adapted from Ref. 54).

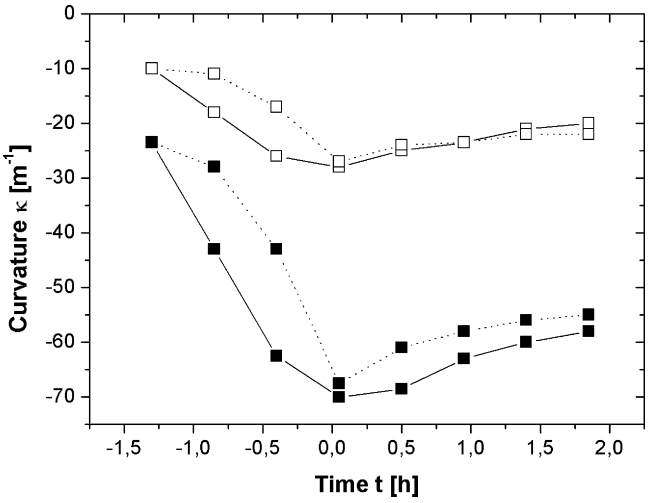

Fig. 9. Measured (solid) and simulated (dashed lines) curvatures of bi-layers of initially 13 μm (open symbols) and 44 μm (full symbols) thick films of undoped zirconia onto a 460 μm thick 3Y-TZP tape. Heating rate of 50 K/h (adapted from Ref. 55).

during constrained sintering may also underestimate substantially the level of real tensile stresses occurring with a non-deformable substrate, as the stresses are relaxed by the substrate curvature.

Cai et al.[13,54] adapted elastic relationships describing the stresses and curling of layered ceramics to viscous materials, as described in Part III. In the case of asymmetric structures, the degree of curvature is related to the mismatch in sintering strain whereas the rate of curvature change is proportional to the mismatch stress, and is therefore a good indicator of the instantaneous stress state. According to the developed framework, relative viscosities of individual materials have a significant effect, for example, if one viscosity is much higher than the other one, warpage may be reduced. Viscous parameters used in this approach can be measured on bulk specimens or derived from theoretical models. The effect of stresses on densification and grain growth is however not considered.

The above approach has been first successfully applied during heating ramp and isothermal hold to laminated zirconia-alumina layered composites,[13] see Fig. 8. It has been extensively used for screen printed $LaSrMnO_3$-yttria stabilized zirconia YSZ or NiO–YSZ on YSZ tapes for SOFC,[119] LTCC and multilayer capacitor systems[120–124] as well as alumina bi-layers with different green densities.[125] It is important to realize there are other possible origins for warpage. For example, binder burnout can lead to bending if the binder is not homogeneously distributed over the tape height.[126] Curvature may also be affected by the formation of a new phase. For example, spinel was formed in layered alumina/magnesia composites.[127]

Kanters' approach[55] was validated on bi-layered structures made of nanocrystalline zirconia tapes with a density mismatch. Viscous constants calculations were taken from the solid-state sintering model of Svoboda and Riedel[29,30] but other models or experimental data can be used if available. As shown in Fig. 9, curvature was predicted to a good agreement for a heating rate of 50 K/h. More complex structures (for example three different material layers) can be described with this model. Current models on the evolution of curvature do not yet have effects of anisotropy included.

4.2.2. Film shrinkage

Measurement of the film shrinkage inside a furnace is an experimental challenge, due to the high-temperature environment and high resolution required for the measuring system. Contrary to curvature measurements, precision given by optical dilatometers is usually not sufficient to follow film shrinkage during constrained sintering, unless really thick films are investigated. Classical contact dilatometers are not also ideal tools for that characterization. Special attention has to be paid to the fact that the measuring system should not affect the sintering of the film (negligible load should be applied on the surface). Usual room temperature methods like ellipsometry (for thinner films) and reflectance spectroscopy or white light interferometer (for thicker films) are inefficient here, due to (i) refractive index changes when porosity decreases and (ii) radiations emitted by the sample at high temperature which may strongly bias the measured spectra. Another solution is the direct observation of a fractured film with a scanning electron microscope to measure its thickness before and after sintering. However, this simple procedure is time consuming and does not allow continuous measurement.

Garino and Bowen[128,129] used an ingenious laser reflectance apparatus to follow thickness changes under isothermal conditions of constrained films. The laser beam was deviated by a mirror inclined due to the height difference between substrate and film top surface. Lu's co-workers[118,130] as well as Jean's group[131] updated this system to compare the densification kinetics of gold or silver paste and glass ceramic composite films deposited on silicon substrates. An alternative system uses a rocking arm amplifying the height difference between substrate and film surface.[132] A vertical laser scanner measures the gap between the bottom alumina substrate and the rocking arm. The

isothermal shrinkage behaviour of 20–150 μm thick alumina films was measured by this technique.

Two general conclusions can be drawn from these studies: (i) for polycrystalline films (zinc oxide, alumina, etc.), densification is not only retarded, but is also really impeded by the constraining conditions, (ii) for sintering of glass films, the isotropic predictions are good at least qualitatively whereas large discrepancies are observed for films densifying by solid-state sintering.[129,118,132] Several explanations for this have been proposed (modified grain growth in constrained films, change of densification mechanism, anisotropy development) which require thorough microstructural characterization.

4.2.3. Microstructural characterization

Bordia and Scherer [16] foresaw in their review article the possible effect of constrained sintering conditions and sintering with rigid inclusions on the microstructure. They suggested that a geometrical constraint might lead to different neck sizes and grain sizes parallel and normal to the substrate/inclusion. Nevertheless these assumptions had not been validated by experimental characterization until very recently. There is also a need to define parameters to characterize and quantify the preferential orientation of features.

It has been shown on alumina,[87] zirconia[133] and LTCC[134] compacts that a uniaxial compressive stress induces anisotropy in the microstructure. In particular, pores tend to align along the loading direction. Furthermore, in the extreme case of zero radial shrinkage sinter-forging experiments,[99] as shown in Fig. 10, the ratio of average grain sizes measured normal and axial to the load is higher than for free sintered specimens. In contrast, compacts sintered freely show an isotropic microstructure and almost random pore orientation. This stress-induced anisotropy can be neglected if the load level and the time during that load application are small.

Only few experimental works deal with the microstructural characterization of constrained films. Choe et al.[118] observed roughly a similar grain size between constrained and free gold layers, but without any quantitative measurements. Lin and Jean found that due to limited densification grain size of constrained silver films is smaller than that of free sintering for comparable sintering times.[131] Stech et al.[112] sintered titania thin films (65 and 140 nm thick) with an initial particle size of 8 nm and measured the sintering trajectory, which is dependent on the film thickness. Grain coarsening took place from the very beginning of sintering so that above a density of about 90%, films consist of a monolayer of grains. Recently, Guillon et al.[135] carried out an extensive characterization of alumina films constrained by an alumina substrate. The sintering trajectory was similar to that observed for specimens sintered freely. Grain anisometry induced by constrained sintering was limited, possibly because of limited grain growth at the studied densities. The choice of another parameter such as neck size ratio may be more sensitive than grain size to highlight changes in microstructure. On the other hand, image analysis of polished cross-sections in the thickness plane revealed a continuous anisotropy development, as pores become more elongated and align preferentially along the thickness direction with increasing density in contrast to films freely sintered (Fig. 11). This anisotropic microstructure may explain why constrained thin films cannot be accurately mod-

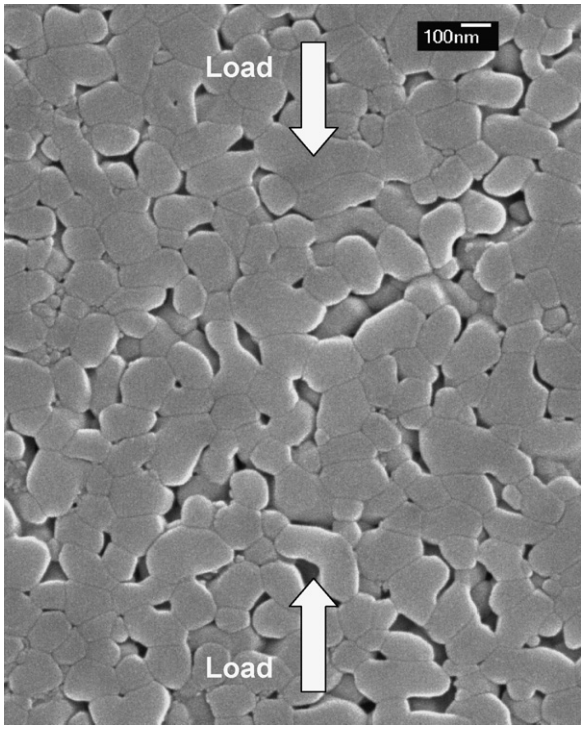

Fig. 10. Microstructure of uniaxially loaded alumina compact (zero radial shrinkage up to ~80% density), grain size ratio 1.12 (0.99 for a compact sintered freely).[99]

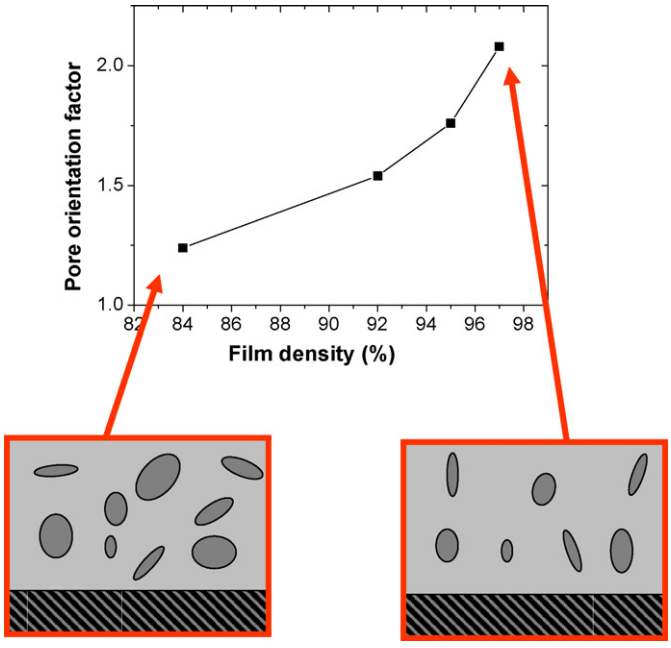

Fig. 11. Pore orientation factor as a function of density for constrained alumina thin films. Higher values indicate preferential orientation along thickness (a value of 1 is characteristic for isotropic microstructure) (adapted from Ref. 135).

elled by using data experimentally obtained for bulk isotropic specimens.[132]

A further complication arises in sintered films, where microstructural gradients have been identified. Calata et al.[130] observed the development of very coarse pores at the interface compared to the rest of the cordierite glass film, which may result from the constraining conditions but also from poor wetting of the substrate by the glass. Sintering LTCC layers on alumina substrate, Mohanram et al.[70] found that the density of residual pores was higher near the interface than in the bulk, probably because the tensile stress that arises from the in-plane constraint may be highest at the interface. Ozer et al.[86] observed a density gradient in alumina tapes containing oriented platelets: the matrix was denser close to the edge of the platelets and porous along the basal planes. This result was also confirmed for alumina films[136]: a thin interface layer was observed in regions where the density was lower and grain size was smaller than elsewhere in the film. This observation may be attributed to the hindrance of particle rearrangement for particles near the substrate, due to friction against gliding and rotation. To complete our understanding, the effect of nature and roughness of the substrate on the constraining conditions should be investigated.

Apart from observing 2D sections, a few 3D characterization tools are available. In situ high-resolution X-ray computed microtomography has been used successfully to monitor microstructural changes during sintering, especially when particles are still identifiable. This non-destructive technique uses X-ray radiographies of a rotating specimen, from which a 3D representation of local attenuation coefficient (which varies accordingly to composition) is computed by means of special algorithms.[137] Currently, the best synchrotron beams enable a voxel size of about 0.3 μm to be attained. In order to catch fine details and extract reliable information from the measurements, microstructural characteristic features have to be large enough compared to the voxel size. Interesting in situ investigations have been carried out on the free sintering of coarse metal,[10,138] glass and ceramic powders.[139] Properties difficult to extract from 2D cross-sections such as spatial distribution of neck size or 3D pore conformation can be obtained. Such a method is readily adapted for fundamental studies of sintering, but it is limited to materials with a coarse microstructure. Better resolution can be obtained from dual beam FIB (focused ion beam) investigations, in which a section of the sintered structure can be removed by ion beam machining. It enables 3D reconstruction from the ablated sections with the resolution of a SEM but sample preparation is destructive.[140]

Nevertheless, density gradients can be assessed by X-ray computed microtomography.[80,141] In this case, the required resolution of the tomographic apparatus is well below the microstructural length scale and gives access to the local internal density distribution. A 3D density map can be derived from the measured differences in X-ray transmission levels (Fig. 12). Such information is useful to characterize the homogeneity of the sintering body and quantify density gradients due to compaction or co-sintering of thick bi-layers and can be used as input data for finite-element analysis.[80]

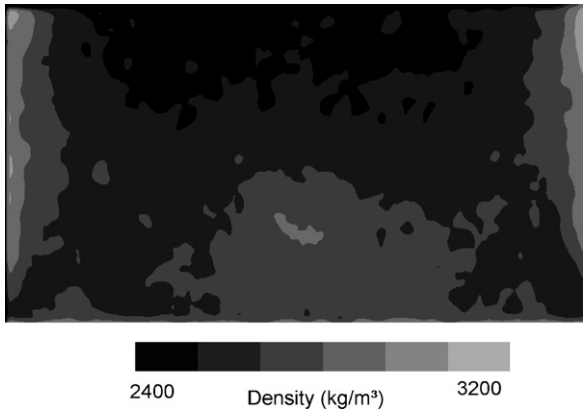

Fig. 12. Density gradients evaluated in a green specimen by means of X-ray computed microtomography (adapted from Ref. 80).

5. Future developments

We identify three areas for future development, one on the macroscale, related to processing, and two on the microscale. There is now acceptable agreement between theory and experiment where densification of the single-phase ceramic with isotropic microstructure is concerned. An exemplary comparison for sintering potential as determined from theory and experiment has been provided in Fig. 5. As the theoretical treatment typically starts with the assumption of a certain powder packing geometry, salient details of processing technology typically cannot be captured. Sintering theory therefore needs to develop into a branch of processing theory where models can in detail describe how powder packing during slip casting, tape casting, etc. evolves. At the same time, the experimentalists need to provide details of the green body (pore size distribution, grain size distribution, distribution of defects) as a function of process technology and density to provide a viable opportunity of verification for the simulation.

A more detailed look at microstructure unveils two further deficits. As already mentioned, there is a need for experimental and theoretical work covering the area of sintering of anisotropic microstructures. This requires treatment of evolution of microstructure under strain incompatibility and deviatoric stresses, as well as densification and grain growth for anisotropic microstructures. Anisotropy may evolve due to anisometric microstructural features, but may also be preferred in order to optimize microstructure. There are examples both for structural[142] as well as functional materials[143] where an anisotropic microstructure offers much improved properties. Therefore, studies in this field, do not only describe arising problems during processing, but also opportunities for property improvement.

Finally, properties based on an average microstructure (density, elastic modulus, etc.) can be well described, as can be the evolution of well-defined large pores.[144] However, crack and damage evolution under complex sintering conditions is envisaged as future area for development. This may include failure due to cracking but also missed tolerances due to edge effects or defects around vias or electrode edges in multilayer structures.

Acknowledgements

We acknowledge helpful discussions with Emil Aulbach and Jean-Baptiste Ollagnier. DG was supported financially through an Alexander-von-Humboldt award.

References

1. Exner, H. E., Principles of single phase sintering. *Reviews on Powder Metallurgy and Physical Ceramics*, *vol. 1*. Freund Publishing House, Tel Aviv, 1979.
2. Exner, H. E., Solid-state sintering: critical assessment of theoretical concepts and experimental methods. *Powder Metall. Int.*, 1980, **4**, 203–209.
3. Exner, H. E. and Arzt, E., Sintering processes. In *Physical Metallurgy*, *vol. 3*, ed. R. W. Cahn and P. Haasen. 4th ed. Elsevier Science, Amsterdam, 1996, pp. 2628–2662.
4. German, R. M., *Sintering Theory and Practice*. John Wiley & Sons, New York, 1996.
5. Kingery, W. D., Bowen, H. K. and Uhlmann, D. R., *Introduction to Ceramics* (*2nd ed.*). John Wiley & Sons, New York, 1976.
6. Rahaman, M. N., *Ceramic Processing and Sintering* (*2nd ed.*). Marcel Dekker, New York, 2006.
7. Kang, S-J. L., *Sintering Densification, Grain Growth and Microstructure*. Butterworth Heinemann, 2004.
8. Olevsky, E. A., Theory of sintering: from discrete to continuum. *Mater. Sci. Eng. R*, 1998, **23**, 41–100.
9. Kraft, T. and Riedel, H., Numerical simulation of solid state sintering; model and application. *J. Eur. Ceram. Soc.*, 2004, **24**(2), 345–361.
10. Lame, O., Bellet, D., Di Michiel, M. and Bouvard, D., Bulk observation of metal powder sintering by X-ray synchrotron microtomography. *Acta Mater.*, 2004, **52**, 977–984.
11. Evans, A. G., Perspective on the development of high-toughness ceramics. *J. Am. Ceram. Soc.*, 1990, **73**, 187–206.
12. Wilcox Sr., D. L., Burdon, J. W., Changrani, R., Chou, C.-F., Dai, S., Koripella, R., Oliver, R., Sadler, M., Allmen, D., Zenhausern, P. and Add Ceramic, F., Add ceramic "MEMS" to the pallet of microsystems technologies. *Mater. Res. Soc. Symp. Proc.*, 2002, **687**, 225–242.
13. Cai, P. Z., Green, D. J. and Messing, G. L., Constrained densification of alumina/zirconia hybrid laminates. I. Experimental observations of processing defects. *J. Am. Ceram. Soc.*, 1997, **80**(8), 1929–1939.
14. Bordia, R. K. and Scherer, G. W., On constrained sintering. I. Constitutive model for a sintering body. *Acta Metall.*, 1988, **36**(9), 2393–2397.
15. Bordia, R. K. and Scherer, G. W., On constrained sintering. II. Comparison of constitutive models. *Acta Metall.*, 1988, **36**(9), 2397–2409.
16. Bordia, R. K. and Scherer, G. W., On constrained sintering. III. Rigid inclusions. *Acta Metall.*, 1988, **36**(9), 2411–2416.
17. Cai, P. Z., Messing, G. L. and Green, D. J., Determination of the mechanical response of sintering compacts by cyclic loading dilatometry. *J. Am. Ceram. Soc.*, 1997, **80**(2), 445–452.
18. Mohanram, A., Messing, G. L. and Green, D. J., Densification and sintering viscosity of low-temperature co-fired ceramic. *J. Am. Ceram. Soc.*, 2005, **88**(10), 2681–2685.
19. Scherer, G. W., Sintering of inhomogeneous glasses: application to optical wavelengths. *J. Non-Cryst. Sol.*, 1979, **34**, 239–256.
20. Scherer, G. W., Sintering of low-density glasses. *J. Am. Ceram. Soc.*, 1977, **60**, 236.
21. Mackenzie, J. K. and Shuttleworth, R., A phenomenological theory of sintering. *Proc. Phys. Soc. B*, 1949, **62**, 833–852.
22. Skorohod, V. V., *Rheological Basis of the Theory of Sintering*. Kiev, Naukova Dumka, 1972.
23. Bassani, J. L. and Linear, Densification and microcracking in sintering compacts. *Mech. Mater.*, 1991, **12**, 119–130.
24. Qian, A., Duva, J. M. and Wadley, H. N. G., Pore shape effects during consolidation processing. *Acta Metall.*, 1996, **44**, 4815–4824.
25. McMeeking, R. M. and Kuhn, L., A diffusional creep law for powder compacts. *Acta Metall. Mater.*, 1992, **40**, 961–969.
26. Cocks, A. C. F., The structure of constitutive laws for the sintering of fine-grained materials. *Acta Metall. Mater.*, 1994, **42**(7), 2191–2210.
27. Swinkels, F. B. and Ashby, M. F., A second report on sintering diagrams. *Acta Metall.*, 1983, **29**, 259–281.
28. Helle, A. S., Easterling, K. E. and Ashby, M. F., Hot isostatic pressing diagrams: new developments. *Acta Metall. Mater.*, 1985, **33**(12), 2163–2174.
29. Svoboda, J., Riedel, H. and Zipse, H., Equilibrium pore surfaces, sintering stresses and constitutive equations for the intermediate and late stages of sintering. I. Computation of equilibrium surfaces. *Acta Metall. Mater.*, 1994, **42**, 435–443.
30. Riedel, H., Zipse, H. and Svoboda, J., Equilibrium pore surfaces, sintering stresses and constitutive-equations for the intermediate and late stages of sintering. 2. Diffusional densification and creep. *Acta Metall.*, 1994, **42**(2), 445–452.
31. Jagota, A., Mikeska, K. R. and Bordia, R. K., Isotropic constitutive model for sintering particle packings. *J. Am. Ceram. Soc.*, 1990, **73**(8), 2266–2273.
32. Du, Z. Z. and Cocks, A. C. F., Constitutive models for the sintering of ceramic components. I. Materials models. *Acta Metall. Mater.*, 1992, **40**(8), 1969–1979.
33. Hsueh, C. H., Evans, A. G., Cannon, R. M. and Brook, R. J., Viscoelastic stresses and sintering damage in heterogeneous powder compacts. *Acta Metall. Mater.*, 1986, **34**(5), 927–936.
34. Bouvard, D. and Meister, T., Modeling bulk viscosity of powder aggregate during sintering. *Model. Sim. Mater. Sci. Eng.*, 2000, **8**, 377–388.
35. Rahaman, M. N. and De Jonghe, L. C., Sintering of CdO under low applied stress. *J. Am. Ceram. Soc.*, 1984, **67**(10), C205–C207.
36. Chu, M.-Y., De Jonghe, L. C. and Rahaman, M. N., Effect of temperature on the densification/creep viscosity during sintering. *Acta Metall.*, 1989, **37**(5), 1415–1420.
37. Rahaman, M. N., De Jonghe, L. C. and Brook, R. J., Effect of shear stress on sintering. *J. Am. Ceram. Soc.*, 1986, **69**(1), 53–58.
38. Rahaman, M. N., De Jonghe, L. C. and Hsueh, C. H., Creep during sintering of porous compacts. *J. Am. Ceram. Soc.*, 1986, **69**(1), 58–60.
39. Rahaman, M. N., De Jonghe, L. C., Scherer, G. W. and Brook, R. R., Creep and densification during sintering of glass powder compacts. *J. Am. Ceram. Soc.*, 1987, **70**(10), 766–774.
40. Rahaman, M. N. and De Jonghe, L. C., Sintering of spherical glass powder under a uniaxial stress. *J. Am. Ceram. Soc.*, 1990, **73**(3), 707–712.
41. Raj, R. and Bordia, R. K., Sintering behavior of Bi-modal powder compacts. *Acta Metall.*, 1984, **32**(7), 1003–1019.
42. Ducamp, V. C. and Raj, R., Shear and densification of glass powder compacts. *J. Am. Ceram. Soc.*, 1989, **72**(5), 798–804.
43. Venkatachari, K. R. and Raj, R., Shear deformation and densification of powder compacts. *J. Am. Ceram. Soc.*, 1986, **69**(6), 499–506.
44. Bordia, R. K. and Raj, R., Sintering of TiO_2–Al_2O_3 composites: a model experimental investigation. *J. Am. Ceram. Soc.*, 1988, **71**(4), 302–310.
45. Gillia, O., *Phenomenological Modelling of Sintering and Numerical Simulation of Industrial Sintering of Cemented Carbide and Alumina*. PhD thesis. Institut National Polytechnique de Grenoble, France, 2000.
46. Gillia, O., Josserond, C. and Bouvard, D., Viscosity of WC–Co compacts during sintering. *Acta Mater.*, 2001, **49**, 1413–1420.
47. Chang, J., Guillon, O., Rödel, J. and Kang, S-J. L., Uniaxial viscosity of gadolinium-doped ceria determined by discontinuous sinter forging. *J. Eur. Ceram. Soc.*, 2007, **27**, 3127–3133.
48. De Jonghe, L. C., Rahaman, M. N. and Hsueh, C. H., Transient stresses in bimodal compacts during sintering. *Acta Metall.*, 1986, **34**(7), 1467–1471.
49. Sudre, O. and Lange, F. F., Effect of inclusions on densification. I. Microstructural development in an Al_2O_3 matrix containing a high volume fraction of ZrO_2 inclusions. *J. Am. Ceram. Soc.*, 1992, **75**(3), 519–524.
50. Sudre, O., Bao, G., Fan, B. and Lange, F. F., Effect of inclusions on densification. II. Numerical model. *J. Am. Ceram. Soc.*, 1992, **75**(3), 525–531.
51. Sudre, O. and Lange, F. F., The effect of inclusions on densification. III. The desintering phenomenon. *J. Am. Ceram. Soc.*, 1992, **75**(12), 3241–3251.
52. Stauffer, D. and Aharony, A., *Introduction to Percolation Theory*. Taylor and Francis, London, 1994.
53. Sahini, M., *Applications of Percolation Theory*. Taylor and Francis, London, 1994.

54. Cai, P. Z., Green, D. J. and Messing, G. L., Constrained densification of Al_2O_3/ZrO_2 hybrid laminates. II. Viscoelastic stress calculations. *J. Am. Ceram. Soc.*, 1997, **80**(8), 1940–1948.
55. Kanters, J., Eisele, U. and Rödel, J., Cosintering simulation and experimentation: case study of nanocrystalline zirconia. *J. Am. Ceram. Soc.*, 2001, **84**(12), 2757–2763.
56. Bordia, R. K. and Raj, R., Sintering behavior of ceramic films constrained by a rigid substrate. *J. Am. Ceram. Soc.*, 1985, **68**(6), 287–292.
57. Scherer, G. W. and Garino, T., Viscous sintering on a rigid substrate. *J. Am. Ceram. Soc.*, 1985, **68**(4), 216–220.
58. Hsueh, C. H., Sintering of a ceramic film on a rigid substrate. *Scripta Metall.*, 1985, **19**, 1213–1217.
59. Jagota, A. and Hui, C. Y., Mechanics of sintering thin films. I. Formulation and analytical results. *Mech. Mater.*, 1990, **9**, 107–119.
60. Jagota, A. and Hui, C. Y., Mechanics of sintering thin films. II. Cracking due to self stress. *Mech. Mater.*, 1990, **9**, 221–234.
61. Mohanram, A., Lee, S.-H., Messing, G. L. and Green, D. J., A novel use of constrained sintering to determine the viscous Poisson's ratio of densifying materials. *Acta Mater.*, 2005, **53**(8), 2413–2418.
62. Carroll, D. R. and Rahaman, M. N., An initial stage model for the sintering of constrained polycrystalline thin films. *J. Eur. Ceram. Soc.*, 1994, **15**(5), 473–479.
63. Wakai, F. and Aldinger, F., Equilibrium configuration of particles in sintering under constraint. *Acta Mater.*, 2003, **51**(3), 641–652.
64. Bordère, S., Gendron, D. and Bernard, D., Improvement in the accuracy of calculated interface morphologies within Monte Carlo simulations of sintering processes. *Scripta Mater.*, 2006, **55**(3), 267–270.
65. Zhao, Y. and Dharani, L. R., Theoretical model for the analysis of a ceramic thin-film sintering on a non-sintering substrate. *Thin Solid Films*, 1994, **245**, 109–114.
66. Olevsky, E. A., Tikare, V. and Garino, T., Multi-scale study of sintering: a review. *J. Am. Ceram. Soc.*, 2006, **89**(6), 1914–1922.
67. Rabe, T., Schiller, W. A., Hochheimer, T., Modes, C. and Kipka, A., Zero shrinkage of LTCC by self-constrained sintering. *Int. J. Appl. Ceram. Technol.*, 2005, **2**(5), 374–382.
68. Lautzenhiser, F. and Amaya, E., Self-constrained LTCC tapes. *Am. Ceram. Soc. Bull.*, 2002, **81**(10), 27–32.
69. Tzeng, S. Y. and Jean, J. H., Stress development during constrained sintering of alumina/glass/alumina sandwich structure. *J. Am. Ceram. Soc.*, 2002, **85**(2), 335–340.
70. Mohanram, A., Lee, S.-H., Messing, G. L. and Green, D. J., Constrained sintering of low temperature Co-fired ceramics. *J. Am. Ceram. Soc.*, 2006, **84**(6), 1923–1929.
71. Reeve, K. D., Non-uniform shrinkage in sintering. *Am. Ceram. Soc. Bull.*, 1963, **42**(8), 452.
72. Evans, A. G., Considerations of inhomogeneity effects in sintering. *J. Am. Ceram. Soc.*, 1982, **65**(10), 497–501.
73. Lange, F. F., Processing-related fracture origins. I. Observations in sintered and isostatically hot-pressed Al_2O_3/ZrO_2 composites. *J. Am. Ceram. Soc.*, 1983, **66**(6), 396–398.
74. Lange, F. F. and Metcalf, M., Processing-related fracture origins. II. Agglomerate motion and crack-like internal surfaces caused by differential sintering. *J. Am. Ceram. Soc.*, 1983, **66**(6), 398–406.
75. Lange, F. F., Davis, B. I. and Aksay, I. A., Processing-related fracture origins. III. Agglomerate motion and crack-like internal surfaces caused by differential sintering. *J. Am. Ceram. Soc.*, 1983, **66**(6), 407–408.
76. Dynys, F. W. and Halloran, J. W., Influence of aggregates on sintering. *J. Am. Ceram. Soc.*, 1984, **67**(9), 596–601.
77. Olevsky, E. A. and Tikare, V., Combined macro–meso scale modeling of sintering. Part I. Continuum approach. *NATO Sci. Ser., Sub-Ser. III: Comput. Syst. Sci.*, 2001, **176**, 85–93.
78. Tikare, V., Olevsky, E. A. and Braginsky, M. V., Combined macro–meso scale modeling of sintering. Part II. Mesoscale simulations. *NATO Sci. Ser., Sub-Ser. III: Comput. Syst. Sci.*, 2001, **176**, 94–104.
79. Schoenberg, S. E., Green, D. J. and Messing, G. L., Effect of green density on the thermo-mechanical properties of a ceramic during sintering. *J. Am. Ceram. Soc.*, 2006, **89**(8), 2448–2452.
80. Schoenberg, S. E., Messing, G. L., Segall, A. E., Grader, A. S., Halleck, P. M. and Green, D. J., Stresses and distortion due to green density gradients during densification. *J. Am. Ceram. Soc.*, 2006, **89**(10), 3027–3033.
81. Dhurjati, R. and Green, D. J., Sintering stresses and warpage produced by density differences in bi-layer structures. *J. Eur. Ceram. Soc.*, 2006, **26**(1–2), 17–25.
82. Boccaccini, A. R. and Olevsky, E. A., Processing of platelet-reinforced glass matrix composites: effect of inclusions on sintering anisotropy. *J. Mater. Proc. Technol.*, 1999, **96**(1–3), 92–101.
83. Boccaccini, A. R., Trusty, P. A. and Taplin, D. M. R., Anisotropic shrinkage of barium-magnesium aluminosilicate glass powder compacts during sintering. *Mater. Lett.*, 1995, **24**, 199–205.
84. Zavaliangos, A. and Bouvard, D., Numerical simulation of anisotropy in sintering due to prior compaction. *Int. J. Powder Metall.*, 2000, **36**(7), 58–65.
85. Raj, P. M. and Cannon, W. R., Anisotropic shrinkage in tape-cast alumina: role of processing parameters and particle shape. *J. Am. Ceram. Soc.*, 1999, **82**(10), 2619–2625.
86. Ozer, I. O., Suvaci, E., Karademir, B., Missiaen, J. M., Carry, C. P. and Bouvard, D., Anisotropic sintering shrinkage in alumina ceramics containing oriented platelets. *J. Am. Ceram. Soc.*, 2006, **89**(6), 1972–1976.
87. Zuo, R., Aulbach, E., Bordia, R. K. and Rödel, J., Critical evaluation of hot forging experiments: case study in alumina. *J. Am. Ceram. Soc.*, 2003, **86**(7), 1099–1105.
88. Bordia, R. K., Zuo, R., Guillon, O., Salamone, S. M. and Rödel, J., Anisotropic constitutive laws for sintering bodies. *Acta Mater.*, 2006, **54**, 111–118.
89. Jagota, Dawson, P. R. and Jenkins, J. T., An anisotropic continuum model for the sintering and compaction of powder packings. *Mech. Mater.*, 1988, **7**, 255–269.
90. Raj, P. M., Odulena, A. and Cannon, W. R., Anisotropic shrinkage during sintering of particle-oriented systems—numerical simulation and experimental studies. *Acta Mater.*, 2002, **50**(10), 2559–2570.
91. Zhou, H. and Derby, J. F., Three-dimensional finite-element analysis of viscous sintering. *J. Am. Ceram. Soc.*, 1998, **81**(3), 533–540.
92. Olevsky, E. and Skorohod, V., Deformation aspects of anisotropic-porous bodies sintering. *J. Phys. IV*, 1993, **3**, 739–742.
93. Olevsky, E. A., Kushnarev, B., Maximenko, A., Tikare, V. and Braginsky, M., Modelling of anisotropic sintering in crystalline ceramics. *Phil. Mag.*, 2005, **85**(19), 2123–2146.
94. Tikare, V., Braginsky, M., Olevsky, E. and Johnson, D., Numerical simulation of anisotropic shrinkage in a 2D compact of elongated particles. *J. Am. Ceram. Soc.*, 2005, **88**(1), 59–65.
95. Ch'ng, H. N. and Pan, J., Modelling microstructural evolution of porous polycrystalline materials and a numerical study of anisotropic sintering. *J. Comput. Phys.*, 2005, **204**, 430–461.
96. Zavaliangos, A., Missiaen, J. M. and Bouvard, D., Anisotropy in shrinkage during sintering. *Sci. Sinter.*, 2006, **38**(1), 13–25.
97. Martin, C. L., Schneider, L. C. R., Olmos, L. and Bouvard, D., Discrete element modeling of metallic powder sintering. *Scripta Mater.*, 2006, **55**(5), 425–428.
98. Henrich, B., Wonisch, A., Kraft, T., Moseler, M. and Riedel, H., Simulations of the influence of rearrangement during sintering. *Acta Mater.*, 2007, **55**(2), 753–762.
99. Wonisch, A., Guillon, O., Kraft, T., Moseler, M., Riedel, H. and Rödel, J., Stress-induced anisotropic behaviour of sintering alumina: discrete element modelling and experiments. *Acta Mater.*, 2007, **55**(15), 5187–5199.
100. Aulbach, E., Zuo, R. and Rödel, J., Laser-assisted high resolution loading dilatometer and applications. *Exp. Mech.*, 2004, **44**(1), 71–75.
101. Aulbach, E., Zuo, R. and Rödel, J., Experimental determination of sintering stresses and sintering viscosities. *Acta Mater.*, 2003, **51**, 4563–4574.
102. Ollagnier, J.-B., Guillon, O. and Rödel, J., Effect of anisotropic microstructure on the viscous properties of a LTCC material. *J. Am. Ceram. Soc.*, 2007, **90**(12), 3846–3851.
103. Mohanram, A., Messing, G. L. and Green, D. J., Measurement of viscosity of densifying glass-based systems by isothermal cyclic loading dilatometry. *J. Am. Ceram. Soc.*, 2004, **87**(2), 192–196.

104. Zuo, R., Aulbach, E. and Rödel, J., Viscous Poisson's coefficient determined by discontinuous hot forging. *J. Mater. Res.*, 2003, **18**(9), 2170–2176.
105. Raj, R., Analysis of the sintering pressure. *J. Am. Ceram. Soc.*, 1987, **70**(9), C210–C211.
106. Zuo, R., Aulbach, E. and Rödel, J., Continuum mechanical approach to sintering of nanocrystalline zirconia. *Adv. Eng. Mater.*, 2005, **7**(10), 949–952.
107. Zuo, R., Aulbach, E. and Rödel, J., Temperature dependence of constitutive behavior for solid state sintering of alumina. *Acta Mater.*, 2004, **52**(10), 3059–3067.
108. Guillon, O., Bordia, R. K. and Rödel, J., Effect of green state processing on the sintering stress and viscosity of alumina compacts. *J. Am. Ceram. Soc.*, 2007, **90**(5), 1637–1640.
109. Salamone, S. M., Stearns, L. C., Bordia, R. K. and Harmer, M. P., Effect of rigid inclusions on the densification and constitutive parameters of liquid-phase sintered $YBa_2Cu_3O_{6+x}$ powder compacts. *J. Am. Ceram. Soc.*, 2003, **86**(6), 883–892.
110. Ostrowski, T., Ziegler, A., Bordia, R. K. and Rödel, J., Evolution of Young's modulus, strength and microstructure during liquid phase sintering. *J. Am. Ceram. Soc.*, 1998, **81**(7), 1852–1860.
111. Ostrowski, T. and Rödel, J., Evolution of mechanical properties of porous alumina during hot pressing. *J. Am. Ceram. Soc.*, 1999, **82**(11), 3080–3086.
112. Stech, M., Reynders, P. and Rödel, J., Constrained film sintering of nanocrystalline TiO_2. *J. Am. Ceram. Soc.*, 2000, **83**(8), 1889–1896.
113. Chang, J., Guillon, O., Kang, S. J. and Rödel, J., Determination of viscoelastic properties of Cd-doped ceria and NiO/YSZ composite; its application to prediction of co-firing behaviour, in preparation.
114. Imanaka, Y., *Multilayered Low Temperature Cofired Ceramics (LTCC) Technology*. Springer, New York, 2005.
115. Singh, P. and Minh, N. Q., Solid oxide fuel cells: technology status. *Int. J. Appl. Ceram. Technol.*, 2004, **1**(1), 5–15.
116. Boccaccini, A. R. and Hamann, B., In situ high-temperature optical microscopy. *J. Mater. Sci.*, 1999, **34**(22), 5419–5436.
117. Lu, G. Q., Sutterlin, R. C. and Gupta, T. K., Effect of mismatched sintering kinetics on camber in a low-temperature cofired ceramic package. *J. Am. Ceram. Soc.*, 1993, **76**(8), 1907–1914.
118. Choe, J. W., Calata, J. N. and Lu, G. Q., Constrained-film sintering of a gold circuit paste. *J. Mater. Res.*, 1995, **10**(4), 986–994.
119. Lee, S. H., Messing, G. L. and Green, D. J., Warpage evolution of screen printed multilayer ceramics during co-firing. *Key Eng. Mater.*, 2004, **264–268**, 321–328, Part 1–3.
120. Jean, J. H., Chang, C. R. and Chen, Z. C., Effect of densification mismatch on camber development during co-firing of nickel-based multilayer ceramic capacitors. *J. Am. Ceram. Soc.*, 1997, **80**(9), 2401–2406.
121. Jean, J. H. and Chang, C. R., Camber development during the co-firing ag-based low-dielectric constant ceramic package bi-layer glass-based dielectric laminate. *J. Mater. Res.*, 1997, **12**(10), 2743–2750.
122. Chang, J. C. and Jean, J. H., Camber development during the cofiring of bi-layer glass-based dielectric laminate. *J. Am. Ceram. Soc.*, 2005, **88**(5), 1165–1170.
123. Hsu, R. T. and Jean, J. H., Key factors controlling camber behavior during the cofiring of bi-layer ceramic dielectric laminates. *J. Am. Ceram. Soc.*, 2005, **88**(9), 2429–2434.
124. Choi, Y. J., Park, J. H., Ko, W. J., Hwang, I. S., Park, J. H. and Park, J. G., Co-firing and shrinkage matching in low- and middle-permittivity dielectric compositions for a low-temperature co-fired ceramics system. *J. Am. Ceram. Soc.*, 2006, **89**(2), 562–567.
125. Ravi, D. and Green, D. J., Sintering stresses and distortion produced by density differences in bi-layer structures. *J. Eur. Ceram. Soc.*, 2006, **26**, 17–25.
126. Hagymasi, M., Roosen, A., Karmazin, R., Dernovsek, O. and Haas, W., Constrained sintering of dielectric and ferrite LTCC tape composites. *J. Eur. Ceram. Soc.*, 2005, **25**(12), 2061–2064.
127. Kim, C. S., Lombardo, S. J. and Winholtz, R. A., Effect of processing on the microstructure and induced-strain mismatch in magnesia-alumina-layered composites. *J. Am. Ceram. Soc.*, 2006, **89**(9), 2718–2725.
128. Garino, T. and Bowen, H. K., Deposition and sintering of particle films on a rigid substrate. *J. Am. Ceram. Soc.*, 1987, **70**(11), C-315–C-317.
129. Garino, T. and Bowen, H. K., Kinetics of constrained-film sintering. *J. Am. Ceram. Soc.*, 1990, **73**(2), 251–257.
130. Calata, J. N., Matthys, A. and Lu, G. Q., Constrained-film sintering of cordierite glass-ceramic on silicon substrate. *J. Mater. Res.*, 1998, **13**(8), 2234–2341.
131. Lin, Y. C. and Jean, J. H., Constrained sintering of silver circuit paste. *J. Am. Ceram. Soc.*, 2004, **87**(2), 187–191.
132. Guillon, O., Aulbach, E., Bordia, R. K. and Rödel, J., Constrained sintering of alumina thin films: comparison between experiment and modelling. *J. Am. Ceram. Soc.*, 2007, **90**(6), 1733–1737.
133. Frame, D. and Bordia, R. K., Stress assisted sintering: evolution of anisotropic microstructures. In *Proc. 4th Int. Conf. Sintering*, ed. D. Bouvard. Grenoble, France, 2005, pp. 272–274.
134. Ollagnier, J.-B., Guillon, O. and Rödel, J., Viscosity of LTCC determined by discontinuous sinter-forging. *Int. J. Appl. Ceram. Technol.*, 2006, **3**(6), 437–441.
135. Guillon, O., Weiler, L. and Rödel, J., Anisotropic microstructural development during the constrained sintering of dip-coated alumina thin films. *J. Am. Ceram. Soc.*, 2007, **90**(5), 1394–1400.
136. Guillon, O., Krauß, S. and Rödel, J., Influence of thickness on the constrained sintering of alumina films. *J. Eur. Ceram. Soc.*, 2007, **27**, 2623–2627.
137. Maire, E., Colombo, P., Adrien, J., Babout, L. and Biasetto, L., Characterization of the morphology of cellular ceramics by 3D image processing of X-ray tomography. *J. Eur. Ceram. Soc.*, 2007, **27**, 1973–1981.
138. Vagnon, A., Lame, O., Bouvard, D., Di Michiel, M., Bellet, D. and Kapelski, G., Deformation of steel powder compacts during sintering: correlation between macroscopic measurement and in situ microtomography analysis. *Acta Mater.*, 2006, **54**(2), 513–522.
139. Bernard, D., Gendron, D., Heintz, J. M., Bordère, S. and Etourneau, J., First direct 3D visualisation of microstructural evolutions during sintering through X-ray computed tomography. *Acta Mater.*, 2005, **53**, 121–128.
140. Holzer, L., Indutnyi, F., Gasser, P. H., Munch, B. and Wegmann, M., Three-dimensional analysis of porous $BaTiO_3$ ceramics using FIB nanotomography. *J. Microsc.-Oxford*, 2004, **216**, 84–95.
141. Deis, T. A. and Lannutti, J. J., X-ray computed tomography for evaluation of density gradient formation during the compaction of spray-dried granules. *J. Am. Ceram. Soc.*, 1998, **81**(5), 1237–1247.
142. Becher, P. F., Sun, E. Y., Plucknett, K. P., Alexander, K. B., Hsueh, C. H., Lin, H. T., Waters, S. B., Westmoreland, C. G., Kang, E. S., Hirao, K. and Brito, M. E., Microstructural design of silicon nitride with improved fracture toughness. I. Effects of grain shape and size. *J. Am. Ceram. Soc.*, 1998, **81**, 2821–2830.
143. Sabolski, E. M., James, A. R., Kwon, S., Trolier-McKinstry, S. and Messing, G. L., Piezoelectric properties of ⟨0 0 1⟩ textured $Pb(Mg_{1/3}Nb_{2/3})O_3$–$PbTiO_3$ ceramics. *Appl. Phys. Lett.*, 2001, **78**, 2551–2553.
144. Flinn, B. D., Bordia, R. K., Zimmermann, A. and Rödel, J., Effect of defect size on strength of alumina during sintering. *J. Eur. Ceram. Soc.*, 2000, **20**, 2561–2568.